Investigating a Parametric Instability
in the LIGO Test Masses

Hans S. Bantilan

Mathematics and Computer Science / Physics and Astronomy,

Carleton College, Northfield, Minnesota 55057, USA

William P. Kells

LIGO Lab - Physics, Mathematics, and Astronomy

California Institute of Technology, Pasadena, California 91125, USA

(September 22, 2006)

Abstract

We investigate a parametric instability in the LIGO interferometers that has the potential to adversely affect instrument sensitivity. Such an effect arises from the excitation of mirror test-mass acoustic modes by an incident optical field, and the subsequent scattering of the optical carrier mode into a superposition of higher-order optical cavity modes. This instability can be described by a single characteristic quantity termed the parametric gain R. Our work involves developing code to evaluate R for various acoustic and optical field profiles on the surface of a mirror test-mass. FEM software is used to calculate acoustic deformation profiles of an Advanced LIGO test mass, and FFT code is used to numerically simulate relaxed optical fields in an interferometer arm. By determining the R value under different conditions, the extent of parametric instability in the context of LIGO is systematically mapped.

1 Introduction

1.1 Parametric Instability

The LIGO laser interferometer gravitational-wave detectors are reaching higher levels of sensitivity; the recent scientific run S5 has seen a marked improvement in the h(f) strain-noise curves in all detectors currently in operation. Though conventional noise sources such as environmental coupling are still dominant, the relative effects on sensitivity due to other noise sources are increasing. The current work investigates the potential for radiation pressure from the laser optical mode to excite the acoustic modes in a mirror test mass, resulting in a parametric instability under certain conditions. This study gains a particular relevance with the upcoming implementation of Advanced LIGO; given the planned increase in input laser power, it has been predicted that the effects of parametric instability become substantially more significant (1).

Parametric instability in a LIGO interferometer is initially made possible by a non-linear coupling of acoustic and optical waves at the test mass mirror interface medium. The physical mechanism of this coupling is the ponderomotive radiation force acting on the mirror surface. An oscillating surface deformation due to acoustic modes in the test mass produces scattered light in a lower-frequency sideband and a higher-frequency sideband, known as Stokes and anti-Stokes respectively. Thus the ponderomotive force, which is proportional to the square of the total field, is modulated at the acoustic oscillation frequency, resulting in instability under certain conditions.

The process leading to instability can be described heuristically as follows. In the Stokes case, the laser "pumped" mode at frequency ω_0 loses energy to some existing acoustic modes of frequency ω_m. By energy considerations, this interaction gives rise to a scattered optical sideband at a lower frequency $\omega_0 - \omega_m$ (see Figure 1.a.). In the anti-Stokes case, on the other
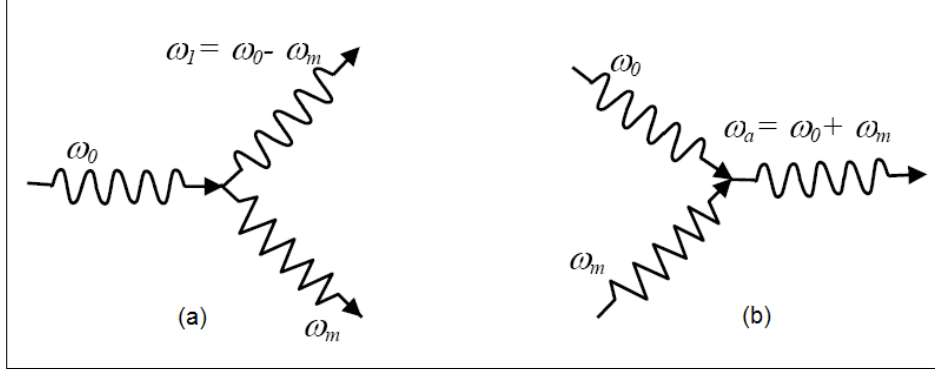
Figure 1: (a) Stokes process; emission of phonons (b) anti-Stokes process; absorption of phonons. Image adapted from (3).

hand,the incident optical wave of frequency ω_0 incident on a test mass absorbs acoustic mode energy, resulting in a scattered optical sideband of a higher frequency $\omega_0 + \omega_m$ (see Figure 1.b.).

The spatial overlapping of three electromagnetic fields with three different frequencies, namely the main optical field of frequency ω_0 and the optical sideband fields of frequencies $\omega_0 \pm \omega_m$, then produces a ponderomotive force impinging on the mirror surface. In fact, it can be readily shown (2) that the modulated ponderomotive force due to Stokes scattering has just the correct frequency and phase to do positive work on the acoustic mode, thus enhancing any incipient acoustic vibration, while the anti-Stokes case results in negative work done, and thus damps such vibrations. The net effect of these two processes determines the level of parametric instability in the test mass under consideration.

1.2 R value

We describe this instability with a quantity denoted as R, which determines a threshold for instability at $R > 1$. This characteristic quantity R is essentially the real part of an eigenvalue for the system of equations describing the acoustic and optical fields.

3

Previous parametric instability work (1) (4) has been done to calculate R values for couplings between an arbitrary acoustic mode and specific higher-order optical modes, in an essentially analytical fashion. This can be done exactly, but it is unfortunately not sufficiently general, since all higher-order modes must be considered in a full calculation of R; under this "mode-pair" formulation, an infinite sum over all optical cavity modes would be necessary.

This can be seen explicitly as follows. Let P be the optical power circulating in the cavity, m mass of the test mass, L cavity length, $\Delta\omega = |\omega_0 - \omega^{s/as}| - \omega_m$ for ω_m, ω_0, ω^s, ω^{as} frequencies of the acoustic and optical modes, Q_m, Q^s, Q^{as} acoustic and optical quality factors, δ^s and δ^{as} relaxation rates of the optical modes, Λ^s and Λ^{as} geometrical overlap factors between the electromagnetic field profile and the acoustic displacement profile; it can be shown that parametric instability can be characterized by the quantity R (1):

$$R = \frac{4PQ_m}{mL\omega_m{}^2 c}\left(\sum_{i=1}^{\infty}\frac{Q_i^s \Lambda_i^s}{1+(\Delta\omega_i^s/\delta_i^s)^2} - \sum_{j=1}^{\infty}\frac{Q_j^{as}\Lambda_j^{as}}{1+(\Delta\omega_j^{as}/\delta_j^{as})^2}\right) \tag{1}$$

the superscripts "s" and "as" refer to "Stokes" and "anti-Stokes" respectively. Note that this expression sums over an infinite number of possible Stokes processes and anti-Stokes processes. A calculation of R that takes into account all these contributions is impractical, not only because of the large number of terms involved but also, more importantly, due to the fact that the quantities Q_i, δ_i, and Λ_i are difficult to determine for every eigenmode in a realistic optical cavity.

In contrast, the numerical procedure presented here is a cavity-mode-independent calculation, such that for each acoustic mode, of surface deformation u, an R value is calculated by considering its coupling to the net optical field. This is done using an FFT code to model the *total* optical field in the cavity, which can be readily decomposed into the main 00 optical mode component, labeled E_0, and the additional field due to acoustic scattering, labeled E_{bk} (see Figure 2). With this notation, the expression for R can be generalized, such
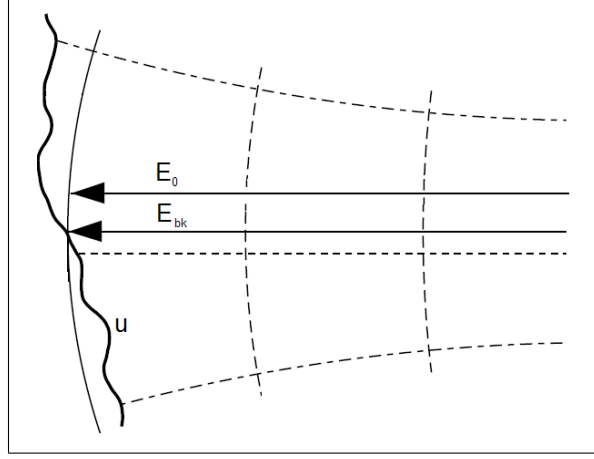
Figure 2: Optical fields impinging on a deformed mirror surface; the mean mirror surface is shown along with acoustic mode deformation u, and optical fields under consideration are labeled E_0 and E_{bk}. Image adapted from (5).

that all optical modes are automatically taken into account, obviating the need for infinite summations (6):

$$R = \frac{4PQ_m}{m\omega_m^2 c} \left(\frac{V \int |E_0^s| Im(E_{bk}^s) u_z dA}{\int |E_0^s|^2 dA \int |\vec{u}|^2 dV} - \frac{V \int |E_0^{as}| Im(E_{bk}^{as}) u_z dA}{\int |E_0^{as}|^2 dA \int |\vec{u}|^2 dV} \right) \qquad (2)$$

where the superscripts "s" and "as" again refer to "Stokes" and "anti-Stokes" respectively, $\int dA$ corresponds to integration over the mirror's front surface, and $\int dV$ corresponds to integration over the mirror's volume. Note that we are calculating static relaxed optical fields which, as discussed in 2.4, simulate the actual dynamic fields.

As with Equation 1, the first term in the expression corresponds to the Stokes contribution R_s, while the second term corresponds to the anti-Stokes contribution R_{as}. It is significant to note, however, that Equation 2 does not preclude R_s or R_{as} from individually being less than 0, whereas Equation 1 does. In fact, there exist explicit single cavity mode examples that predict negative values of R far enough away from resonance (see Section 3).

1.3 Objectives

The goal of this project is to establish the viability of a static relaxed-field numerical calculation of the parametric instability problem, and to then implement this approach on a subset of test mass acoustic modes. Code has been developed to calculate acoustic mode deformation profiles in a test mass (7) and the relaxed optical field circulating in a LIGO interferometer arm cavity (8); these are utilized to form the basis of our R value calculation code.

From Equation 1, one can explicitly see that the R contribution of a given acoustic-optical mode pair is proportional to the overlap factors denoted Λ, and to a resonance factor of the form $\frac{1}{1+(\Delta\omega/\delta)^2}$. It has been shown in previous work (3) that high R values can be caused by the coupling of a given acoustic mode to a single or a few resonant higher-order optical modes. The current work gives a more complete description of the physical situations that give rise to these high R values.

2 Method

2.1 Configuration

The physical system being modeled here consists of a single LIGO interferometer arm with two mirror test masses at its ends (see Figure 3). It is important to note that a dynamical system is being simulated with an essentially static model; though the acoustic mode deformation profiles and optical field profiles are all oscillating in time, only static field maps are used. The test mass under consideration is simulated by a finite-element model that uses
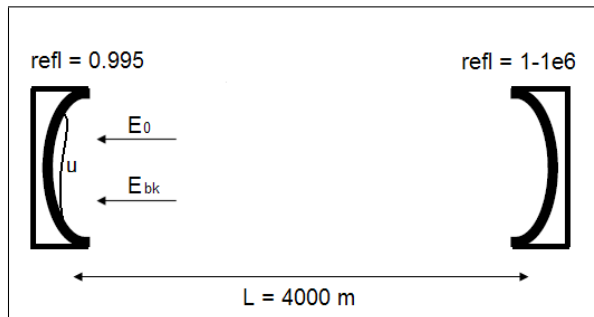

Figure 3: Interferometer cavity arm being modeled.

Advanced LIGO parameters (see Table 1). Only one test mass is modeled with an acoustic deformation; the acoustic modes for different test masses are assumed to be uncorrelated, so that the parametric instability arising from n test masses can be decomposed into n independent single-test-mass problems. It is significant to note here that in the current work, the acoustic mode quality factor Q_m is assumed to have a frequency dependence $Q_m \propto \omega_m^{-0.83}$ such that $Q_m|_{\omega_m=7000Hz} = 10^8$.

The interferometer arm cavity itself is simulated by an FFT code, again using typical Advanced LIGO parameters (see Table 2). The model being used here does not take into account the effects of the power or signal recycling cavities on the scattered field. This has been done in some detail in other work (9) (10), within the restricted context of Equation 1.

Quantity	Value(s)
No. of FEM Nodes	21797
No. of FEM Elements	4752
TM Radius	0.17 m
TM Thickness	0.20 m
TM Flat Length	0.095 m
TM Modulus of Elasticity	7.3×10^{10} Pa
TM Poisson's Ratio	0.17
TM Shear Modulus	3.1×10^{10} Pa
TM Mass Density	2202 kgm^{-3}

Table 1: FEM model, test-mass parameter values used in parametric instability study (Adv LIGO).

Quantity	Value(s)
Laser Wavelength	1.064 μm
Power Circulating in the Cavity	830 kW
Cavity Length	4000 m
Mirror Curvature Radii	2076 m (ITM, ETM)
Mirror Intensity Reflectivities	0.995 (ITM), $1 - 10^{-6}$ (ETM)
Mirror Intensity Transmittivities	0.005 (ITM), 10^{-6} (ETM)
Beam Diameter at Mirror Surface	0.12 m
Mirror Aperture Diameter	0.34 m (ITM, ETM)
Calculational Window Size	0.70 m $\times$ 0.70 m
Maximum No. of Iterations	500
Convergence Proximity Criterion	10^{-6}

Table 2: FFT model, interferometer parameter values used in parametric instability study (Adv LIGO).

2.2 FEM Model

The FEM model of an Advanced LIGO input test mass used in the analysis (see Figure 4) has the properties listed in Table 1. The problem of finding the acoustic mode deformation profiles can then be solved using modal analysis, based on eigenvalue and eigenvector information of the modeled rigid body system under consideration. Let M and K denote the $n \times n$ positive definite matrices for a system with n degrees of freedom; the unforced
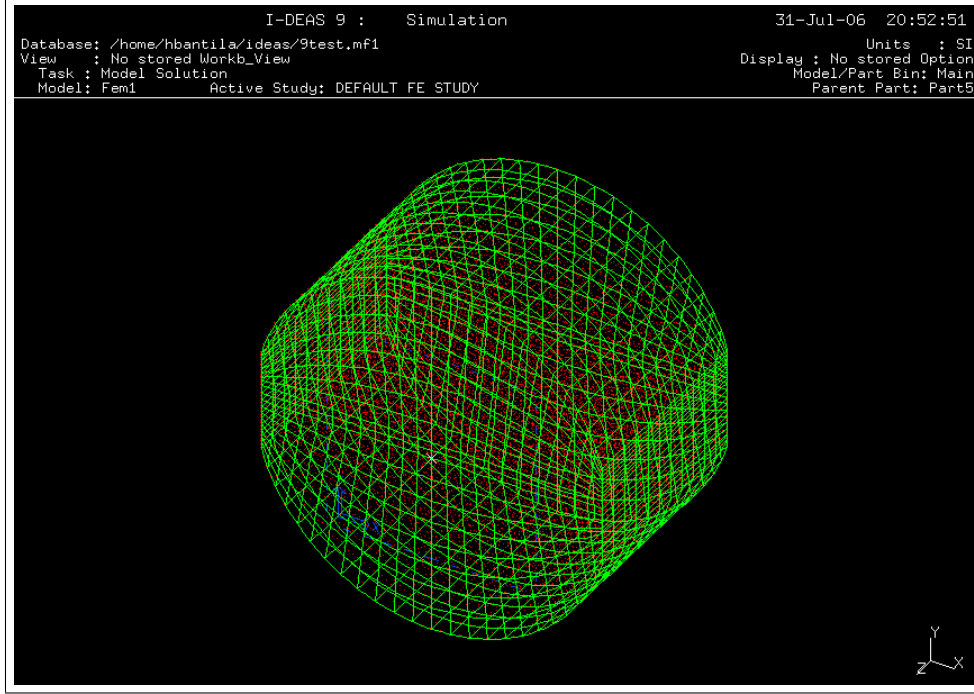
8

Figure 4: I-DEAS finite element model of input test mass.

underdamped response, using generalized coordinates $q(t)$, then has the form:

$$M\ddot{q}(t) + Kq(t) = 0 \tag{3}$$

An ansatz of $q(t) = ue^{i\omega t}$ results in an eigenvalue problem of the usual form:

$$(K - \omega^2 M)u = 0 \tag{4}$$

The acoustic mode shapes u and the eigenfrequencies ω can then be calculated by I-DEAS, using the Lanczos algorithm to solve for the kernel of the matrix $(K - \omega^2 M)$.

2.3 FFT Model

The FFT code used in the analysis models the optical field wavefronts in a LIGO interferometer by taking two-dimensional transverse slices of the beam, normal to the beam propagation axis (see Figure 5). The transverse slice from an initial reference plane at the
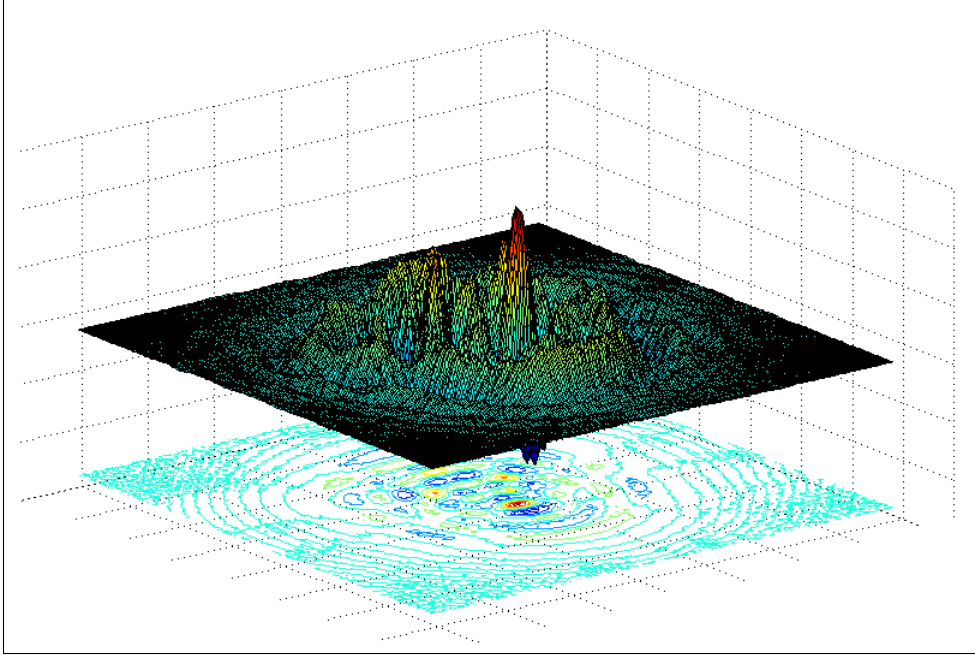
9

Figure 5: A transverse slice of E_{bk} taken at the input test mass; the imaginary part is shown on a 256×256 grid.

input test mass is propagated in the cavity using an FFT method. It is well known that the light in LIGO interferometers satisfies the paraxial approximation; given an optical field of the form $E(x, y, z) = \psi(x, y, z)e^{-ikz}$, with x,y transverse coordinates and z axial coordinate, this approximation stipulates that $|\frac{\partial^2 \psi}{\partial z^2}| \ll |\frac{\partial \psi}{\partial z}|, |\frac{\partial^2 \psi}{\partial z^2}| \ll |\frac{\partial^2 \psi}{\partial x^2}|, |\frac{\partial^2 \psi}{\partial z^2}| \ll |\frac{\partial^2 \psi}{\partial y^2}|.$ It is then straightforward to show that with this approximation, Maxwell's equations lead to the paraxial wave equation:

$$\frac{\partial^2 \psi}{\partial x^2} + \frac{\partial^2 \psi}{\partial y^2} - 2ik\frac{\partial \psi}{\partial z} = 0 \tag{5}$$

where k is the propagation vector of the optical field. Now, a particularly effective way of analyzing the paraxial wave approximation is by way of Huygen's principle, which expresses the transverse optical shape $\psi(x, y, z)$ as an integral of the contributions of an infinite number of spherical waves from point sources, resulting in an integral form (11):

$$\psi(x, y, z) = \frac{i}{L\lambda} \int \int \psi(x_0, y_0, z_0)\kappa(r - r_0)dx_0 dy_0 \tag{6}$$

10

where $r^2 = x^2 + y^2 + z^2$, L is the length of the cavity and λ is the wavelength of the laser light. Notice that this integral has exactly the form of a two-dimensional convolution in x and y of the optical shape $\psi(x_0, y_0, z_0)$ with a spherical wavefunction $\kappa(r - r_0)$. By the convolution theorem, it then follows that the optical shape at any point $\psi(x, y, z)$ can be calculated by successive Fourier transforms F and inverse Fourier transforms F^{-1} (12):

$$\psi(x, y, z) = \frac{i}{L\lambda} F^{-1}(F(\psi(x_0, y_0, z_0))F(\kappa(r - r_0))) \tag{7}$$

2.4 Matlab Code

The approach taken by the current work is numerical in nature, with the primary calculations directly relevant to the parametric instability problem being performed by a code written in Matlab. The acoustic modes are first calculated using the FEM package (see Figure 5). The Matlab code then converts the acoustic deformation profile into a phase map, which is critical to the entire procedure. When an optical wave E_0 is incident on a mirror that has some deformation, $u(x, y)$, it experiences a transverse distortion in phase of the form e^{2iku} due to the deformation, giving rise to an initial scattered wave $E_0 e^{2iku} \approx E_0 + 2iku E_0$. In keeping only terms to first order in u, the scale of the mirror deformation is assumed to be perturbative; the scale used in practice has an RMS value 1 Å. Further note that since only first-order terms are kept, all higher-order scattered light is proportional to $2iku E_0$, regardless of the number of reflections that has occurred in the cavity (see Figure 6).

The aforementioned phase map is designed to simulate exactly this scattered light. The phase distortion due to the mirror deformation is applied to the optical field, by way of a transmission map that is input into the FFT code. This optical field is then propagated by the FFT code and allowed to relax.

Recall that in Equation 2, two components of the relaxed optical fields are required in
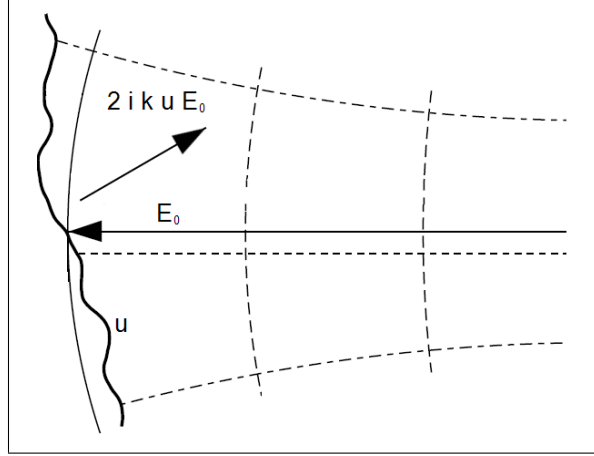
11

Figure 6: Initial scattering of an optical field incident on a deformed mirror surface. Image adapted from (5).

the calculation of R: the main TEM_{00} optical mode component E_0 and the additional field due to acoustic scattering E_{bk}. The E_0 component is found by taking advantage of the fact that the acoustic deformation is perturbative in scale; in effect, the E_0 component of the relaxed field obtained from the FFT code run with a phase map applied is taken to be the same as the total relaxed field obtained from the FFT code with no phase map applied. The E_{bk} component is obtained by subtracting this E_0 field from the total relaxed field E_{tot} obtained from the FFT code run with a phase map applied, so $E_{bk} = E_{tot} - E_0$ (see Figure 7).

The remainder of the code is designed to address the fact that a dynamical system is being simulated with an essentially static model. As was expressed in Section 1, the physical system under consideration involves an optical field encountering an acoustic mode deformation pattern that is oscillating in time. Therefore, the scattered field is distinguished by being different in frequency, namely as $\omega_0 \pm \omega_m$ sidebands. Our static simulation makes no distinction in frequency from a dynamic point of view. However, all that is really significant is the round-trip phase experienced by the fields involved, so one can interpret the difference in frequency between a particular sideband and the main optical wave as a fixed difference in round-trip phase. It is then an excellent approximation to account for this difference in
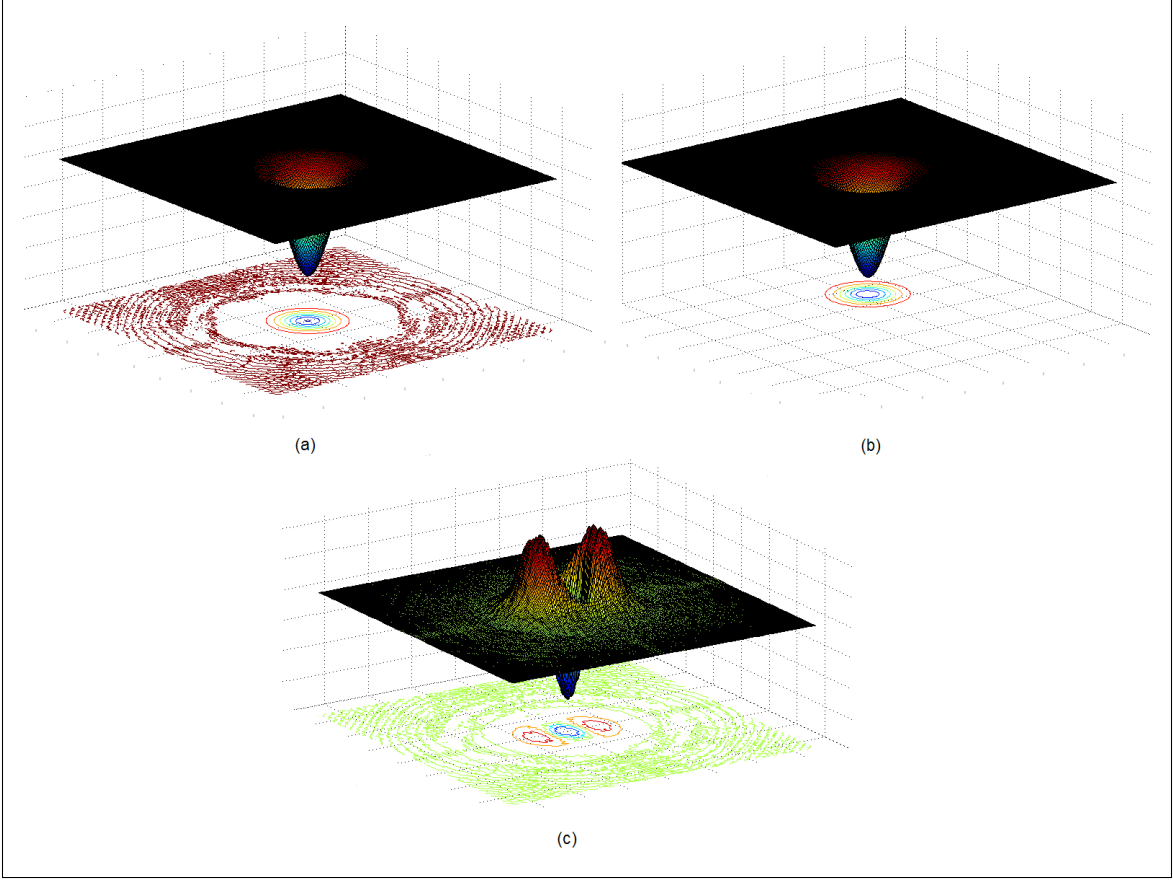
Figure 7: (a) E_{tot} field map (b) E_0 field map (c) E_{bk} field map; this particular example has strong scattering into the Hermite-Gaussian TEM$_{30}$.

round-trip phase by an appropriate microscopic change in the length of the cavity. In the FFT code's calculation of the scattered Stokes field, the cavity length is deliberately made shorter by $\frac{\omega_m}{2\pi}\frac{L}{c}\lambda$. For the anti-Stokes field calculation, the cavity length is deliberately made longer by the same length to account for the fact that it has a higher frequency.

At the end of the entire procedure, the optical field profiles E_0 and E_{bk} along with the acoustic deformation profile u can be used to calculate an R value according to Equation 2.

3   Verification

Verification cases were done in order to validate the R values obtained from the new procedure with known results from previous work. We begin by studying two simple cases, where "synthetic" acoustic deformation profiles are generated such that light is scattered into only the TEM_{00} main cavity mode (Case 1), and only into the Laguerre-Gaussian TEM_{10} (Case 2). We then move on to studying an acoustic mode deformation calculated by the I-DEAS FEM package, that closely corresponds to an acoustic mode studied by a group from the University of Western Australia (3).

3.1   Synthetic TEM_{00} Case

It can be readily shown that a constant "piston" synthetic acoustic deformation scatters light into only the TEM_{00}, since it physically corresponds to a simple change in cavity length. Equation 1 can be used exactly to calculate R_{as} in this single higher-order mode case; the code produced R values that corresponds well to the theoretical curve near resonance, which is the regime in which Equation 1 holds (see Figure 8). The divergent results from formulations Equation 1 and Equation 2 are understood. The $R_{s/as}$ values of Equation 1 must always be positive; however, this is a Lorentzian approximation to the (periodic) cavity resonance. The formulation of Equation 2, correctly taking this into account, predicts negative R_s values that the approximate formulation of Equation 1 does not allow.

3.2   Synthetic TEM_{10} Case

The second case involves a synthetic acoustic deformation with the shape of the generalized Laguerre polynomial $L_1^{(0)}$. It can be shown that this specific shape results scattering into only the Laguerre-Gaussian TEM_{10} (5). Again, the R_{as} values calculated with our code closely agreed to the predicted values near resonance (see Figure 9).
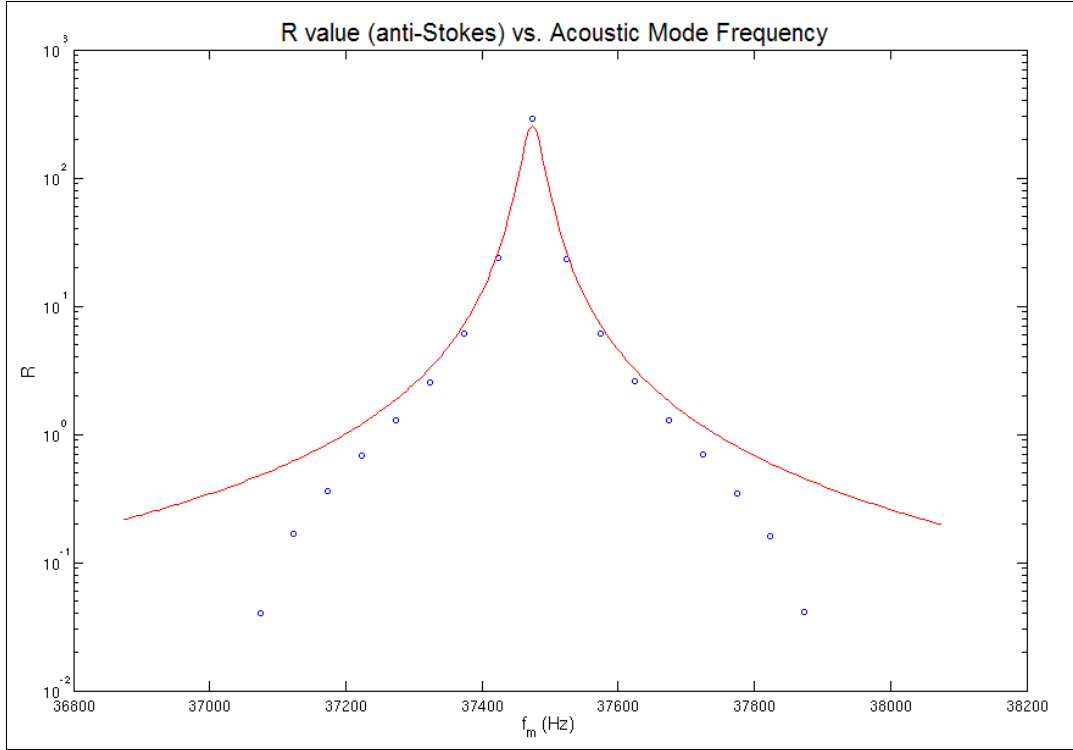
14

Figure 8: R_{as} value (anti-Stokes) vs. acoustic mode frequency for synthetic 00 case; R_{as} calculated with numerical procedure (blue), R_{as} calculated with Equation 1 (red).
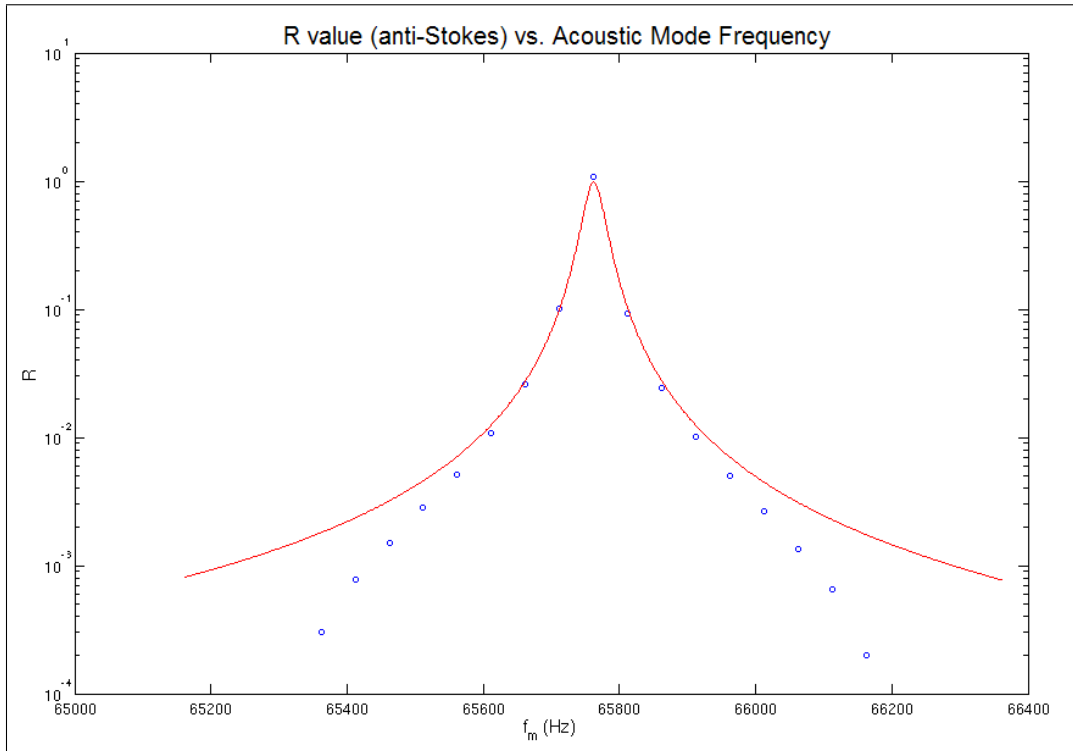

Figure 9: R_{as} value (anti-Stokes) vs. acoustic mode frequency for synthetic 10 case; R_{as} calculated with numerical procedure (blue), R_{as} calculated with Equation 1 (red).

3.3   UWA Group Acoustic Mode Case

An acoustic mode was calculated with the I-DEAS package that has approximately the same shape as an acoustic mode of frequency 28342 Hz that was found by the UWA group (3) (see Figure 10). That group did an R calculation for the coupling between this acoustic

(a)   (b)

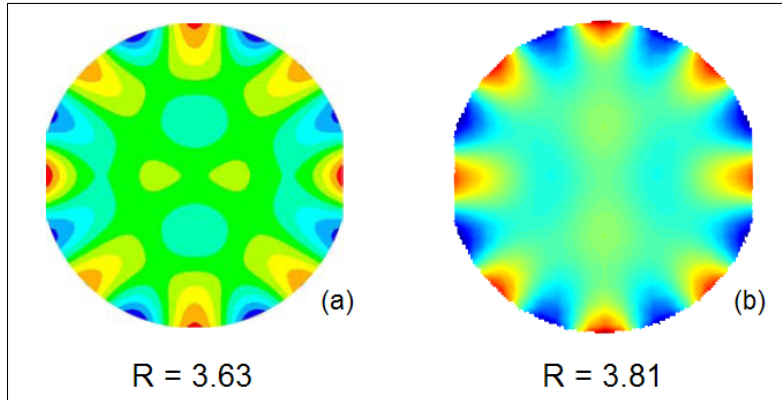R = 3.63   R = 3.81

Figure 10: (a) UWA group acoustic mode and at frequency 28342 Hz (b) Similar acoustic mode at frequency 27518 Hz.

mode and the Laguerre-Gaussian TEM_{10}. Since the acoustic mode frequency 28342 Hz is indeed near the TEM_{10} resonance, one would expect that the total R value would be close to the UWA value of $R = 3.63$. A slight caveat in our comparison to this value is that the frequency of our mode was 27518 Hz. This difference is most likely explained by the unavoidable errors in finite-element modeling as the UWA group used ANSYS, a different FEM package. Fortunately, the UWA group had noted down an angular frequency detuning of $\Delta\omega = 213.6$ Hz, so we forced a similar detuning in our R calculation. We then calculated an R value using our code, and arrived at $R = 3.81$, agreeing with the UWA result to within 5% [1].

---

[1]This $R = 3.81$ was calculated using a constant $Q_m = 10^8$, in accordance with the parameters used in the UWA R calculation which led to $R = 3.63$ (3). Later work by the UWA group factored both the ω_m dependence of the quality factor Q_m, as well as the effects of the power recycling cavity, leading to an R value of $R = 0.5$ (13).

4 Results and Discussion

R values have been generated for acoustic modes between 1 Hz and 90000 Hz (see Figure 11). Surveying these shows that only a few acoustic modes have associated R values greater
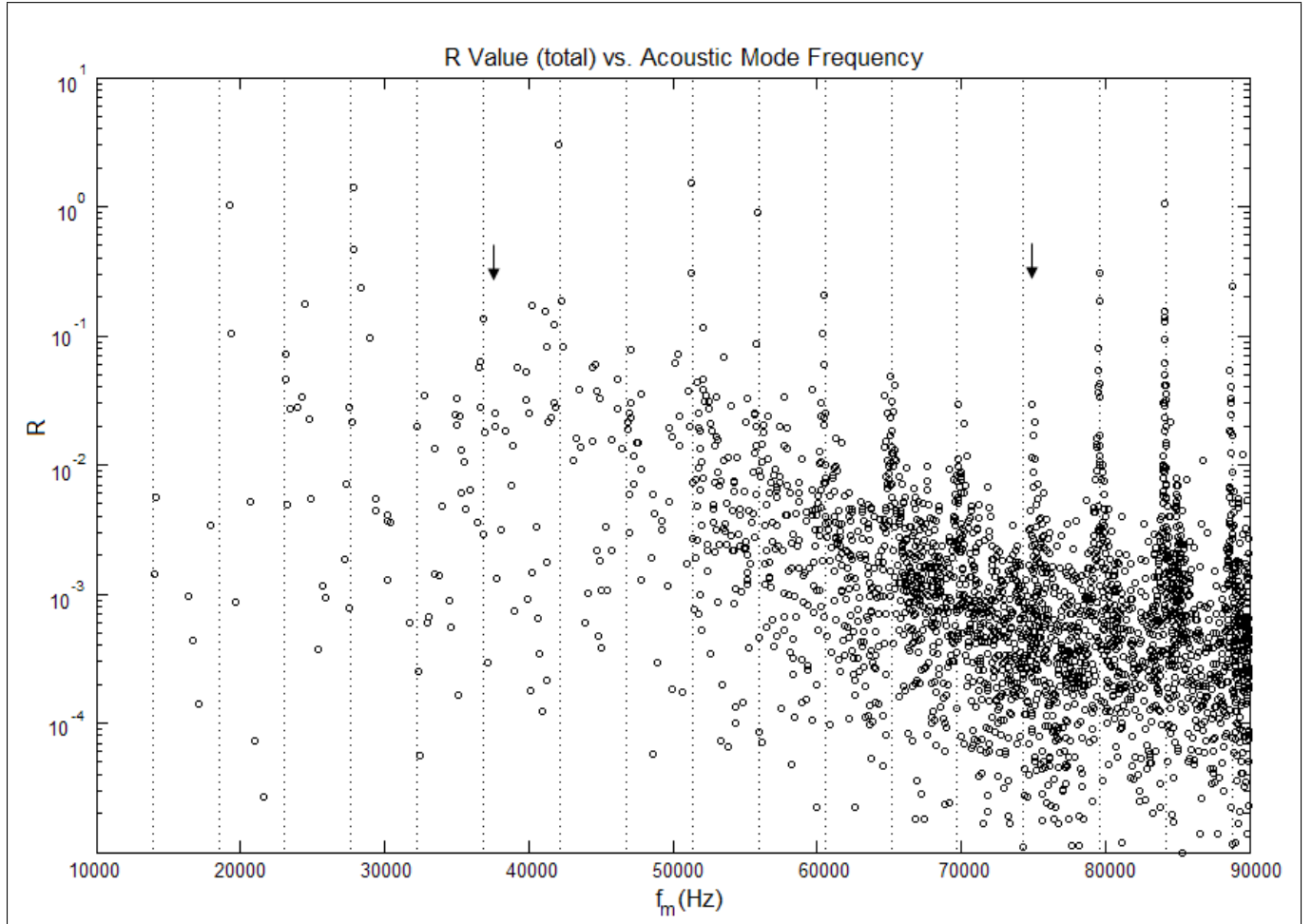

Figure 11: R value (total) vs. acoustic mode frequency; the dotted lines indicate analytically predicted Stokes resonances from order 1 to order 8, according to Equation 12; the arrows indicate multiples of the free spectral range.

than 1. There are a total of 9061 acoustic modes being analyzed, of which 4574 are such that $R > 0$. Recall that the condition for parametric instability is that $R > 1$, where R is defined by Equation 2. All $R > 1$ values in this plot are associated with single higher-order mode resonances. Note that none of the high R values plotted are exactly at a particular higher-order mode resonance frequency; none of the acoustic modes that were calculated by

I-DEAS had an acoustic frequency that was exactly equal to a higher-order mode resonant frequency. Such a coincidence would produce extremely high R values (see Figure 12). The
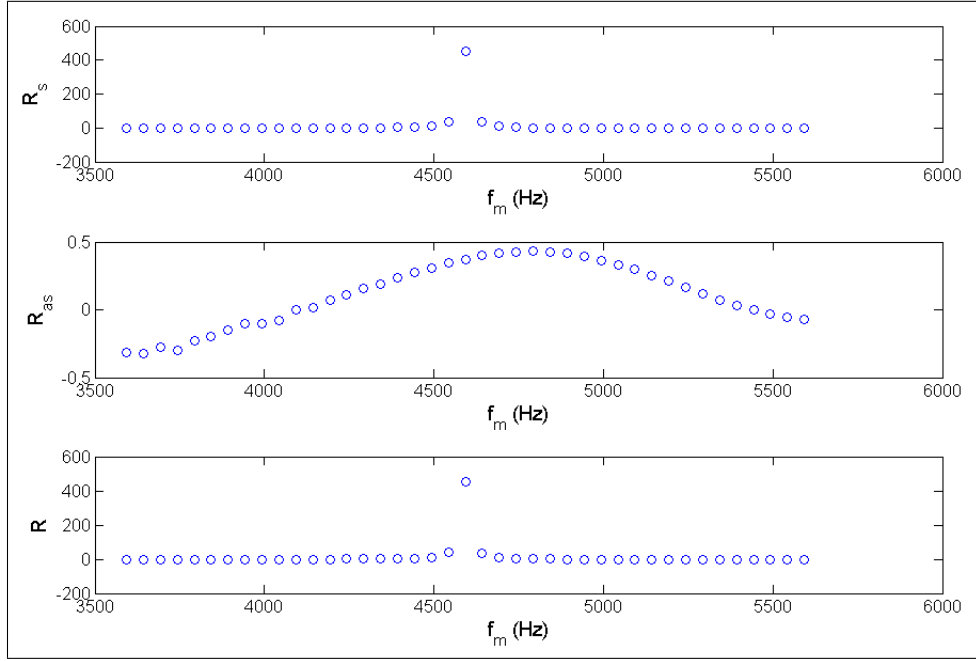

Figure 12: R value vs. acoustic mode frequency for an example near a higher-order mode resonance, with a peak corresponding to a large R value. Note that none of these points appear in Figure 11 as they are points generated by "forcing" the frequency of the acoustic mode to be near a higher-order mode resonant frequency, even though this may be far from the case.

position of these resonances in frequency space can in fact be predicted. Consider the case of a single Laguerre-Gaussian ideal cavity mode of nth order with frequency ω_0; the total phase shift $\phi(z_2 - z_1)$ from one end of the cavity $z = z_1$ to another at $z = z_2$ can then be expressed (11):

$$\phi(z_2 - z_1) = \omega_0 \frac{L}{c} - n(\zeta(z_2) - \zeta(z_1)) \tag{8}$$

where $\zeta(z)$ is the Gouy phase shift. Note that the one-way Gouy phase shift $\zeta(z_2) - \zeta(z_1)$ can be readily shown to be of the form (11):

$$\zeta(z_2) - \zeta(z_2) = cos^{-1}(\pm\sqrt{g_1 g_2}) \tag{9}$$

18

where $g_i = 1 - \frac{L_i}{R_i}$ are the g-factors of the cavity, and the sign of the square root is the same as the sign of the g-factors (in our situation, $g_1 = g_2 = 1 - \frac{L}{R}$). The resonance condition for a standing wave requires this one-way phase shift $\phi(z_2 - z_1)$ to be an integer multiple of π. Now recall that the scattering in our particular case produces a change in frequency from ω_0 to $\omega_0 \pm \omega_m$. Considering only the lower Stokes sideband, the total phase shift $\phi(z_2 - z_1)$ in our physical situation then becomes:

$$\phi(z_2 - z_1) = (\omega_0 - \omega_m)\frac{L}{c} - n\cos^{-1}\left(1 - \frac{L}{R}\right) \tag{10}$$

implying a resonance condition of:

$$(\omega_0 - \omega_m)\frac{L}{c} - n\cos^{-1}\left(1 - \frac{L}{R}\right) = q\pi, \qquad q \in \mathbb{Z} \tag{11}$$

Given that L is chosen such that the main mode at frequency ω_0 is exactly resonant, it then follows that for Stokes scattering, the acoustic frequencies f_m^s at which single higher-order modes are resonant must be the positive real numbers given by the expression:

$$f_m^s = -\frac{qc}{2L} - \frac{c}{2\pi L}n\cos^{-1}\left(1 - \frac{L}{R}\right), \qquad q \in \mathbb{Z} \tag{12}$$

Similarly, for anti-Stokes scattering, the acoustic frequencies f_m^{as} at which single higher-order modes are resonant are the positive real numbers given by:

$$f_m^{as} = \frac{qc}{2L} + \frac{c}{2\pi L}n\cos^{-1}\left(1 - \frac{L}{R}\right), \qquad q \in \mathbb{Z} \tag{13}$$

Looking at the actual transverse field patterns that are being generated for these peak points, one can visually distinguish these dominant modes. Acoustic modes which generate R values near resonance peaks were identified and R vs. f_m plots were generated for each of these by artificially setting the frequency of the acoustic mode to different values. In
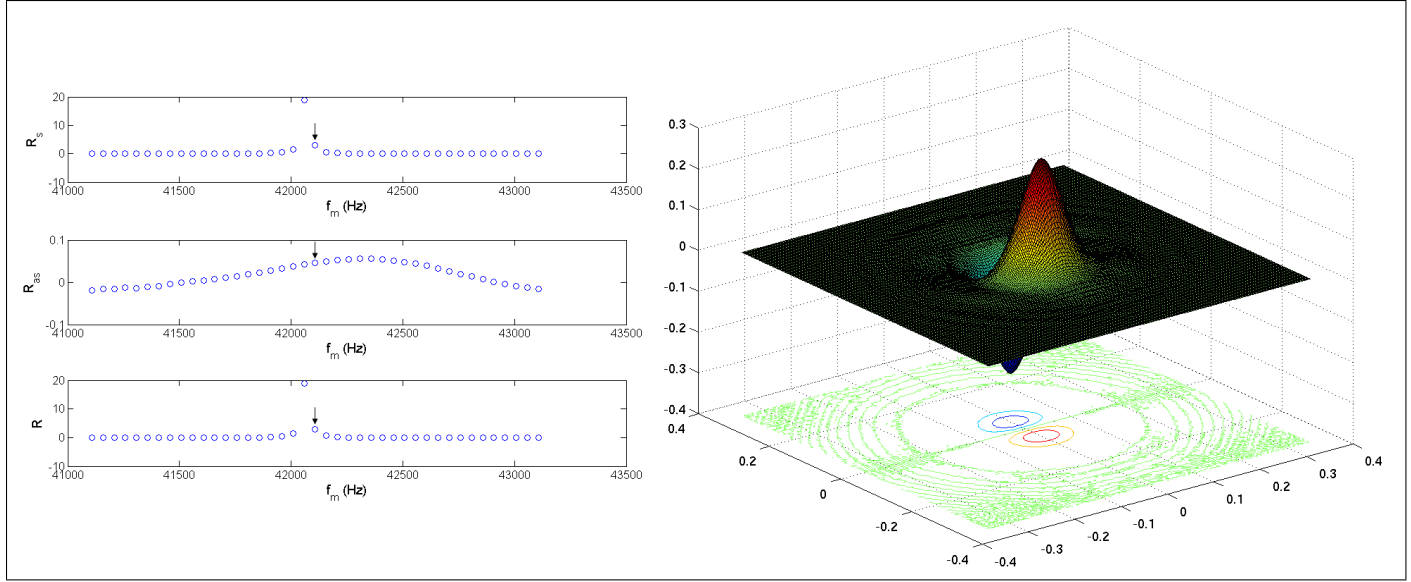
Figure 13: (a) R value vs. acoustic mode frequency for an example near a Stokes resonance at $\omega_m = 42108$ Hz; arrows indicate ω_m (b) optical field map at the input test mass associated with this Stokes resonance.
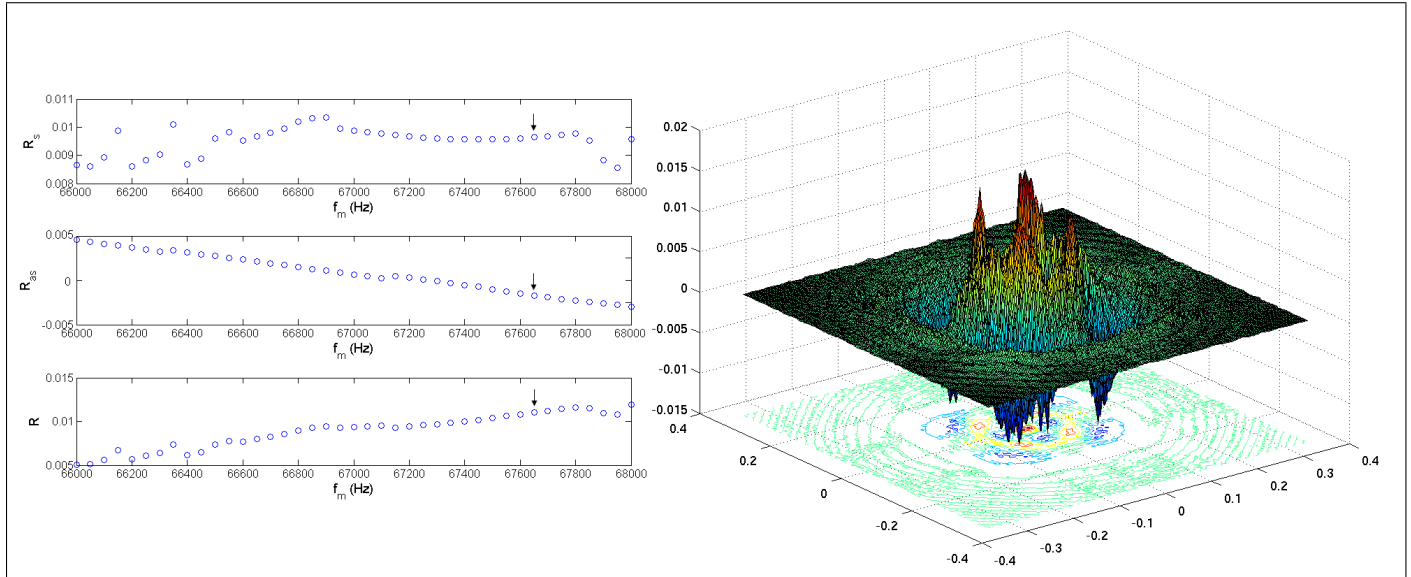

Figure 14: (a) R value vs. acoustic mode frequency for an example far from resonance at $\omega_m = 67661$ Hz; arrows indicate ω_m (b) optical field map at the input test mass associated with a point far from resonance.

addition, the optical field map corresponding to the scattered optical field from each of these acoustic modes were generated. The results for various high R value cases confirm that these high R values are indeed due to dominant single higher-order mode contributions (see Figure 13).

It is then natural to ask if this is generally true. An open question has always been whether high R values can be caused not only by the resonant behavior of a single or a few higher-order optical modes, but by the summed contribution of an infinite number of such modes (14). To answer this question, we examined all non-resonance associated points with high R values, using the same procedure that was implemented on the peak points. The results for a number of such points show a background R level that is below one, but is higher than expected (see Figure 14). In particular, one would expect to see a background R value level on the order of 10^{-3}, which is indeed observed in the synthetic acoustic mode cases (see Section 3).

However, the results from actual acoustic mode cases reveal higher background levels. In fact, we find instances of R values as high as 0.1 in frequency bands devoid of discernable cavity resonances. Therefore it is highly suggestive that we are demonstrating a true background contribution to R, distinct from what can be inferred from sums (such as in Equation 1) over the first few distinct cavity mode resonances. However this cannot be concluded without further validations and consistency checks on the numerical procedures employed here. For instance, we have found certain "numerical backgrounds" in particular results. Results of the kind shown in Figures 13 and 14 ought to be (as a strict feature of the formulation of Equation 2) exactly independent of the mirror surface distortion scale height used in the FFT run that produces E_{bk}. In practice, however, this is not the case. As one might expect, too large a scale height introduces non-linear distortions. Results employing too small a scale height drown in fixed aliasing, finite pixilation, and pseudo-diffraction (finite field map

extent) effects. Carefully optimized examples (Figures 8 and 9) show that the present algorithms can be executed to yield very low ($R < 10^{-4}$) spurious background levels. However this care has not yet been extended to the full set of 9061 acoustic modes calculated. Modest further studies should resolve this background question.

5   Conclusions

We present a numerical method for calculating R values, by considering the coupling between an arbitrary acoustic mode and the net optical field circulating in a single LIGO intereferometer arm. A generalized expression for R was derived and code was written then implemented on all acoustic modes in the frequency range of 1 Hz to 90000 Hz. We arrive at the conclusion that any given point with $R > 1$ is caused by the resonant behavior of a single higher-order optical mode, given the parameters used in the current model. Results also indicate that summed contributions from the infinite number of optical modes present in the cavity may indeed greatly enhance R values, even for points far from resonance.

It is important to note that this entire problem scales to various parameters in Equation 2, including the laser power circulating in the cavity. Though the particular parameters used in this study lead to only a few R values greater than 1, the use of different parameters and an inclusion of the power recycling cavity and the signal recycling cavity in the model can lead to an overall upward shift of the R value curve.

6   Acknowledgements

Acknowledgements go to Dennis Coyne for the test-mass model used in the FEM analysis, and to Hiroaki Yamamoto for the FFT code that was critical to the entire work. The authors would like to thank both for enlightening conversations and invaluable advice.

References

(1) V. B. Braginksy, S. Strigin, and S. Vyatchanin, Phys. Lett. A , 332 (2001).

(2) W. Kells and E. D'Ambrosio, Phys. Lett. A , 326 (2002).

(3) L. Ju, S. Gras, C. Zhao, J. Degallaix, and D. Blair, Investigation on parametric instabilities in advanced ligo, School of Physics, University of Western Australia, 2006.

(4) C. Zhao, L. Ju, J. Degallaix, S. Gras, and D. Blair, Phys. Rev. Lett. **94**, 1 (2005).

(5) Y. Hefetz, N. Mavalvala, and D. Sigg, LIGO Proj. Publ. **LIGO-P960024-A-D**, III (1996).

(6) W. Kells, personal communication.

(7) D. Coyne, personal communication.

(8) H. Yamamoto, personal communication.

(9) V. B. Braginksy, S. Strigin, and S. Vyatchanin, Phys. Lett. A , 111 (2002).

(10) V. B. Braginksy, A. Gurkovsky, S. Strigin, and S. Vyatchanin, Analysis of parametric oscillatory instability in signal recycled ligo interferometer, LIGO Proj. Publ., 2006.

(11) A. Siegman, *Lasers*, University Science Books, 55D Gate Five Road, Sausalito, CA 84865, 1986.

(12) B. Bochner, *Modelling the Performance of Interferometric Gravitational-Wave Detectors with Realistically Imperfect Optics*, PhD thesis, Massachusetts Institute of Technology, 1998.

(13) L. Ju, S. Gras, C. Zhao, J. Degallaix, and D. Blair, Phys. Lett. A **354**, 360 (2006).

(14) P. Savov, K. Thorne, and S. Vyatchanin, LIGO Proj. Publ. **LIGO-G050441-00**, III (2005).